

MULTIWAVELENGTH ANALYSIS OF THE INTRIGUING GRB 061126: THE REVERSE SHOCK SCENARIO AND MAGNETIZATION

A. GOMBOC^{1,2}, S. KOBAYASHI², C. GUIDORZI^{2,3}, A. MELANDRI², V. MANGANO⁴, B. SBARUFATTI⁴, C. G. MUNDELL², P. SCHADY⁵, R. J. SMITH², A. C. UPDIKE⁶, D. A. KANN⁷, K. MISRA^{8,9}, E. ROL¹⁰, A. POZANENKO¹¹, A. J. CASTRO-TIRADO¹², G. C. ANUPAMA¹³, D. BERSIER², M. F. BODE², D. CARTER², P. CURRAN¹⁴, A. FRUCHTER¹⁵, J. GRAHAM¹⁵, D. H. HARTMANN⁶, M. IBRAHIMOV¹⁶, A. LEVAN¹⁷, A. MONFARDINI^{2,18}, C. J. MOTTRAM², P. T. O'BRIEN¹⁰, P. PREMA¹⁹, D. K. SAHU²⁰, I. A. STEELE², N. R. TANVIR¹⁰, K. WIERSEMA¹⁰

Draft version October 29, 2018

ABSTRACT

We present a detailed study of the prompt and afterglow emission from *Swift* GRB 061126 using BAT, XRT, UVOT data and multi-color optical imaging from ten ground-based telescopes. GRB 061126 was a long burst ($T_{90} = 191$ s) with four overlapping peaks in its γ -ray light curve. The X-ray afterglow, observed from 26 min to 20 days after the burst, shows a simple power-law decay with $\alpha_X = 1.290 \pm 0.008$. Optical observations presented here cover the time range from 258 s (Faulkes Telescope North) to 15 days (Gemini North) after the burst; the decay rate of the optical afterglow shows a steep-to-shallow transition (from $\alpha_1 = 1.48 \pm 0.06$ to $\alpha_2 = 0.88 \pm 0.03$) approximately 13 min after the burst. We suggest the early, steep component is due to a reverse shock and show that the magnetic energy density in the ejecta, expressed as a fraction of the equipartition value, is a few ten times larger than in the forward shock in the early afterglow phase. The ejecta might be endowed with primordial magnetic fields at the central engine. The optical light curve implies a late-time break at about 1.5 days after the burst, while there is no evidence of the simultaneous break in the X-ray light curve. We model the broad band emission and show that some afterglow characteristics (the steeper decay in X-ray and the shallow spectral index from optical to X-ray) are difficult to explain in the framework of the standard fireball model. This might imply that the X-ray afterglow is due to an additional emission process, such as late time central engine activity rather than blast-wave shock emission. The possible chromatic break at 1.5 days after the burst would give support to the additional emission scenario.

Subject headings: gamma rays: bursts - cosmology: observations

1. INTRODUCTION

Facilitated by the rapid accurate localization and dissemination of observed properties of Gamma Ray Bursts (GRBs) by the *Swift* satellite (Gehrels et al. 2004), multiwavelength studies of GRBs are providing important insights into the physics of these prodigious cosmic explosions (Zhang 2007; Mészáros 2006; Piran & Fan 2007). Despite the diverse range of observed properties of GRBs when studied over a large time range in wavebands spanning the electromagnetic spectrum, the primary goals of multiwavelength analyses are to understand the physical origin of prompt and afterglow emission, to challenge current theoretical models, to determine the nature of the expanding fireball and the role played by magnetic fields in driving the explosion.

The combination of γ -ray, X-ray, optical and ultraviolet data from *Swift* instruments with deep, early-time optical imaging from rapid-response ground-based robotic telescopes, such as the Faulkes and Liverpool telescopes, as well as later-time observations with 4- and 8-m class telescopes has provided unprecedented datasets for the investigation of GRB physics.

Here we present a detailed analysis of a set of multi-

Electronic address: andreja.gomboc@mf.uni-lj.si, (ag, sk, crg, axm, cgm, rjs, dfb, mfb, dxc, am, cjm, ias)@astro.livjm.ac.uk

¹ Faculty of Mathematics and Physics, University of Ljubljana, Jadranska 19, SI-1000 Ljubljana, Slovenia.

² Astrophysics Research Institute, Liverpool John Moores University, Twelve Quays House, Birkenhead, CH41 1LD, UK.

³ INAF - Osservatorio Astronomico di Brera, via Bianchi 46, 23807 Merate (LC), Italy.

⁴ INAF - Istituto di Astrofisica Spaziale e Fisica Cosmica di Palermo, via Ugo La Malfa 153, 90146 Palermo, Italy.

⁵ The UCL Mullard Space Science Laboratory, Holmbury St Mary, Dorking, Surrey RH5 6NT, UK.

⁶ Department of Physics and Astronomy, Clemson University, Clemson, SC 29634, USA.

⁷ Thüringer Landessternwarte Tautenburg, Sternwarte 5, 07778 Tautenburg, Germany.

⁸ Aryabhata Research Institute of Observational Sciences, Manora Peak, Nainital 263 129, India.

⁹ Inter University Center for Astronomy and Astrophysics (IUCAA), Post Bag 4, Ganeshkhind, Pune 411 007, India.

¹⁰ Department of Physics and Astronomy, University of Leicester, Leicester, LE1 7RH, UK.

¹¹ Space Research Institute (IKI), 84/32 Profsoyuznaya Str, Moscow 117997, Russia.

¹² Instituto de Astrofísica de Andalucía (CSIC), P.O. Box 03004, E-18080 Granada, Spain.

¹³ Indian Institute of Astrophysics, Bangalore, 560 034, India.

¹⁴ Astronomical Institute Anton Pannekoek, University of Amsterdam, Kruislaan 403, 1098 SJ Amsterdam, The Netherlands.

¹⁵ Space Telescope Science Institute, 3700 San Martin Drive, Baltimore, MD 21218, USA.

¹⁶ Ulugh Beg Astronomical Institute, Tashkent 700052, Uzbekistan.

¹⁷ Department of Physics, University of Warwick, Coventry CV4 7AL, UK.

¹⁸ CNRS-CTBT, Grenoble 38000, France.

¹⁹ Institute of Astronomy, University of Cambridge, Madingley Road, Cambridge, CB3 0HA, UK.

²⁰ Center for Research and Education in Science & Technology, Hosakote, Bangalore, 562 114, India.

wavelength observations of *Swift* GRB 061126 comprising γ -ray, X-ray, ultraviolet and optical observations from ground- and space-based telescopes that observed the initial prompt emission and early afterglow through to the late stages of the fading afterglow, 15–20 days after the burst. Following the detection of GRB 061126 by *Swift*'s Burst Alert Telescope (BAT), several ground-based telescopes (Raptor-S, Super-LOTIS, NMSU-1m telescope, PAIRITEL, Faulkes Telescope North, KAIT, and 0.3-m telescope at New Mexico Skies Observatory) reacted promptly to the BAT trigger and detected a bright optical and NIR afterglow, with detections being obtained in the first tens to hundreds of seconds after the burst. The *Swift* satellite did not slew immediately to the burst location because of the Earth limb constraint. Therefore, observations with the narrow field instruments, the X-Ray Telescope (XRT) and the UV/Optical Telescope (UVOT), began 26 minutes after the trigger. An associated host galaxy was detected (Rol et al. 2006; Perley et al. 2008) with a redshift $z = 1.1588$ (Perley et al. 2008).

The optical afterglow of GRB 061126 shows a steep-to-flat transition at ~ 13 min after the trigger. Similar flattening has been observed in optical afterglows of GRB 990123 (Akerlof et al. 1999), GRB 021211 (Fox et al. 2003; Pandey et al. 2003; Li et al. 2003), GRB 060117 (Jelinek et al. 2006), and GRB 080319B (Racusin et al. 2008). Particularly, the GRB 021211 occurred at a similar redshift ($z = 1.006$, Vreeswijk et al. 2002) and was linked with a possible supernova (Della Valle et al. 2003). In these cases, the early, steep afterglow was interpreted as due to emission from the reverse shock dominating the light curve, while the later, more slowly fading component as due to the forward shock (Sari & Piran 1999; Nakar & Piran 2005; Wei 2003; Fox et al. 2003; Pandey et al. 2003; Jelinek et al. 2007). Some of these bursts have also shed light on the issue of magnetization of the fireball. It is shown that at the deceleration of a fireball ejecta, the microscopic parameter ϵ_B in the ejecta should be much larger than in the forward shock in the case of GRB 990123 and possibly GRB 021211 (Zhang et al. 2003; Kumar & Panaitescu 2003; Fan et al. 2002).

With its steep-to-shallow optical light curve behavior, GRB 061126 offers a valuable opportunity to investigate the multiwavelength prompt and afterglow properties of a GRB with a prominent reverse shock component, which is not always present in light curves of GRBs with bright optical counterparts (Mundell et al. 2007a). Observations and data reduction are presented in §2; the derived temporal and spectral characteristics of the burst are presented in §3, and in §4 we present and discuss a reverse and forward shock model, implications for the standard model and the magnetization of the fireball.

Throughout this paper we use the following notation for a power-law flux: $F(\nu, t) \propto t^{-\alpha} \nu^{-\beta}$, where α is the temporal decay index, β is the spectral index and it is related to the photon index Γ as $\Gamma = 1 + \beta$. Quoted errors are given at 1σ confidence level, unless stated otherwise.

2. OBSERVATIONS AND ANALYSIS

2.1. Swift BAT data

BAT triggered and localized GRB 061126 (BAT trigger 240766) on 2006 Nov 26, at 08:47:56 UT (Sbarufatti et al. 2006a). We refer to this time as T_0 throughout the

paper. This was a 1.024 s rate-trigger on a long burst with $T_{90} = 191$ s. The BAT light curve in different energy bands is shown in Figure 1.

BAT data were obtained in the burst mode, covering $T_0 - 239$ s to $T_0 + 574$ s (Krimm et al. 2006) and were processed using the HEASOFT software package, version 6.1.2 and version 2.6 of the Calibration DataBase, applying calibration, standard filtering and screening criteria. We extracted the mask-tagged light curves (Figures 1 and 2) with a binning time of 64 ms in the four nominal energy bands adopting the ground-refined coordinates provided by the BAT team (Krimm et al. 2006). We applied the energy calibration using the closest-in-time gain/offset file through the tool `bateconvert`. The light curves are expressed as count rates: these are background-subtracted counts per second per fully illuminated detector for an equivalent on-axis source, as the default corrections are applied: `ndets`, `pcode`, `maskwt`, `flatfield`. We extracted the mask weighted spectrum from $T_0 - 10$ s to $T_0 + 200$ s using the tool `batbinevt`. All required corrections were applied: we updated it through `batupdatephakw` and generated the detector response matrix using `batdrngen`. We then used `batphasyserr` to account for the BAT systematics as a function of energy. Finally we grouped the energy channels of the spectrum by imposing a $5\text{-}\sigma$ threshold on each grouped channel. The spectrum (Figure 3) was fit with XSPEC11.3.

2.2. Swift XRT data

XRT began observing the burst at 09:14:31 UT, i.e. at $T_0 + 1598$ s, and monitored the source until 2006 December 28 at 23:59:57 UT for a total of 29 observation sequences.

XRT data were processed using the HEASOFT package. The XRT exposure times after all the cleaning procedures were 203 s in Window Timing mode (WT) and 271 ks in Photon Counting mode (PC), distributed over a time interval of 32 days. PC data from the first sequence were corrected for pile-up, caused by the relatively high count rate of the source. The XRT light curve (Figure 4) was extracted requiring a minimum signal-to-noise ratio of 3.

The spectral analysis was performed only on the first seven sequences (up to $T_0 + 570$ ks; the source dropped below count rate 3×10^{-3} counts s^{-1} afterwards). Data in three time intervals: WT data from the first sequence (from $T_0 + 1603$ s to $T_0 + 1807$ s), PC data from the first sequence (from $T_0 + 1807$ s to $T_0 + 15280$ s) and PC data from sequences 2-7 (from $T_0 + 15280$ s to $T_0 + 570$ ks), were fitted with an absorbed power-law model using XSPEC version 11.3. Instrumental energy channels below 0.3 keV and above 10 keV for PC and WT spectra were ignored. Data were binned with a requirement of a minimum of 20 photons per bin. Auxiliary response files and exposure maps were created using the HEASOFT software for each segment, and the appropriate response matrixes from the CALDB were applied.

2.3. Swift UVOT data

The UVOT began observing the field of the GRB 061126 at $T_0 + 1605$ s. Observations started with a 9 s settling exposure in *V*-filter, followed by a 100 s

exposure in white light filter. After this the automated sequence rotated six times through the UVOT filters, taking a series of short exposures (*UVW1, U, B, white, UVW2, V, UVM2*; 10 s for white filters and 20 s for the rest). Observations continued with the rotating filter wheel and a combination of exposures of 200 s, 300 s or 900 s up to $T_0 + 50$ ks. Details of the UVOT observation log are in Sbarufatti et al. (2006b).

To improve the signal to noise ratio of the afterglow detection, consecutive images were coadded to create at least 40 s exposures. Photometric measurements were obtained from the UVOT data with the tool *UVOT-SOURCE* (version 2.2) using a circular source extraction region with a $3''$ and $4.5''$ radius for the optical and UV filters, respectively. An aperture correction was then applied to the photometry to maintain compatibility with the current UVOT effective area calibration¹. The background was measured in a source-free region near the target using an extraction radius of $12''$.

To combine UVOT data with ground based observations, we re-calibrated the UVOT B and V values with respect to the 5 field stars detected also in ground based B- and V-band observations. Due to similarity of calibration stars' colors the color correction between UVOT and standard filter magnitudes could not be applied.

2.4. Ground-based Optical data

Observations with ground-based telescopes started shortly after the trigger time: Raptor-S at $T_0 + 20.87$ s (Wren et al. 2006), Super-LOTIS at $T_0 + 35$ s (Williams & Milne 2006), NMSU-1m telescope at $T_0 + 47$ s (Holtzam et al. 2006), PAIRITEL at $T_0 + 58$ s (Bloom 2006), Faulkes Telescope North (FTN) at $T_0 + 258$ s (Smith et al. 2006), KAIT at $T_0 + 356$ s (Perley et al. 2008) and 0.3-m telescope at New Mexico Skies Observatory at $T_0 + 623$ s (Torii 2006). The FTN reacted robotically and using the automatic GRB-pipeline LT-TRAP (Guidorzi et al. 2006), independently detected the fading optical afterglow at the position in agreement with the position from UVOT: R.A.(J2000)=05:46:24.46, Dec(J2000)=+64:12:38.5 ($\pm 0.5''$) (Vanden Berk et al. 2006). Detection of the IR afterglow at a consistent position followed shortly by Bloom (2006).

Observations continued with several telescopes, including the SARA telescope (Updike et al. 2006), the Mt Abu IR Observatory (MIRO) (Baliyan et al. 2006), the Tautenburg Schmidt telescope (TLS) (Kann & Malesani 2006), the Sampurnanand Telescope (ST) (Misra 2006), the Maidanak observatory (MAO) (Pozanenko et al. 2006), the Himalayan Chandra Telescope (HCT), and the Observatorio de Sierra Nevada (OSN) 1.5m telescope. Late time observations ($> T_0 + 1$ day) were performed by the Liverpool Telescope (LT) as part of the *RoboNet-1.0* project² (Gomboc et al. 2006), as well as with the TLS, Isaac Newton Telescope (INT) and Gemini North. Details of the ground-based observations presented in this paper are summarized in Table 1.

Magnitudes in *BVR* bands have been calibrated using Landolt standard field stars (Landolt 1992) observed by the FTN on the same night as the GRB. The night was photometric and the zero point of each optical fil-

ter was stable throughout the entire FTN observational sequence. Photometry was performed using the Starlink GAIA Photometry Tool, carefully selecting the right parameters for each observation acquired with different instruments. Data taken by other telescopes were then cross-calibrated with the FTN observations using several stars in the field to provide a consistent and well-calibrated multi-telescope light curve. Data from the LT, INT and Gemini North, as well as FTN i' -band observations, were calibrated using the SDSS pre-burst (revised) photometry (Cool 2006). Finally, the data were corrected for the Galactic extinction: $E_{B-V} = 0.182$ mag derived from the extinction maps by Schlegel et al. (1998) and $A_V = 0.604$ mag (following Cardelli et al. (1989) we evaluate $A_B = 0.79$ mag, $A_R = 0.49$ mag, $A_{i'} = 0.39$ mag and $A_{g'} = 0.70$ mag). Conversion from magnitudes to flux densities followed Bessel (1979) and Fukugita et al. (1996).

3. RESULTS

3.1. Prompt Gamma-ray Emission

The prompt emission of GRB 061126 shows in all BAT energy bands two main peaks and two smaller ones (Figure 1). The mask-weighted light curves show emission above background level starting at $T_0 - 10$ s. The brightest peak occurs at $T_0 + 7$ s and the last peak, which is also second brightest ends at $\approx T_0 + 25$ s. Low level emission is ongoing to $\approx T_0 + 200$ s resulting in $T_{90}(15 - 350 \text{ keV}) = 191 \pm 10$ s. This γ -ray emission tail is more evident in the logarithmic scale (Figure 2) and can be fitted with a power-law of the form $\propto (t-t_s)^{-\alpha_\gamma}$. Using data points at $t > T_0 + 37$ s (after the last peak), we derive best fit parameters $\alpha_\gamma = 1.3 \pm 0.2$, $t_s = (-2.4 \pm 12.2)$ s with $\chi^2/\text{dof} = 6.9/9$.

We fit the BAT total spectrum with the Band function (Band et al. 1993). Figure 3 shows our best fit, which gives following parameters: low-energy photon index $\alpha_B = -1.05 \pm 0.17$, high energy photon index $\beta_B = -2.3$ (fixed) and $E_p = 197_{-52}^{+173}$ keV at 1σ and 197_{-70}^{+1300} keV at 90% cl. We note that our first value is not consistent with the value of $E_p = 620$ keV derived by Perley et al. (2008), and our latter value is in rough agreement with it. The discrepancy is presumably due to the neglect of soft gamma tail at $> T_0 + 35$ s by Perley et al. (2008).

We compared our estimate of E_p and photon index $\Gamma = 1.34 \pm 0.08$ derived from BAT data with the empirical relation between Γ and E_p found by Zhang et al. (2003), their Figure 2. We find our values in excellent agreement with this relation.

To test the Amati relation, we assume the redshift of $z = 1.1588$ determined by Perley et al. (2008) from the host galaxy spectroscopy. We use standard cosmology ($H_0 = 70 \text{ km s}^{-1} \text{ Mpc}^{-1}$, $\Omega_m = 0.3$ and $\Omega_\Lambda = 0.7$), and derive $E_{p,i} = 425_{-110}^{+370}$ keV and $E_{\text{iso}} = 7.4_{-2.9}^{+0.1} \times 10^{52}$ erg. We find that this burst lies inside, although close to the 2σ border, of the updated Amati relation (see Figure 2 in Amati 2006).

3.2. The X-ray Afterglow

The temporal behavior of the X-ray afterglow, shown in Figure 4, is well described by a single power-law with index $\alpha_X = 1.290 \pm 0.008$; however, we note that the large value of the $\chi^2/\text{dof} = 198.2/99$, reflects the presence

¹ <http://heasarc.gsfc.nasa.gov/docs/caldb/swift/docs/uvot/>

² <http://www.astro.livjm.ac.uk/RoboNet/>

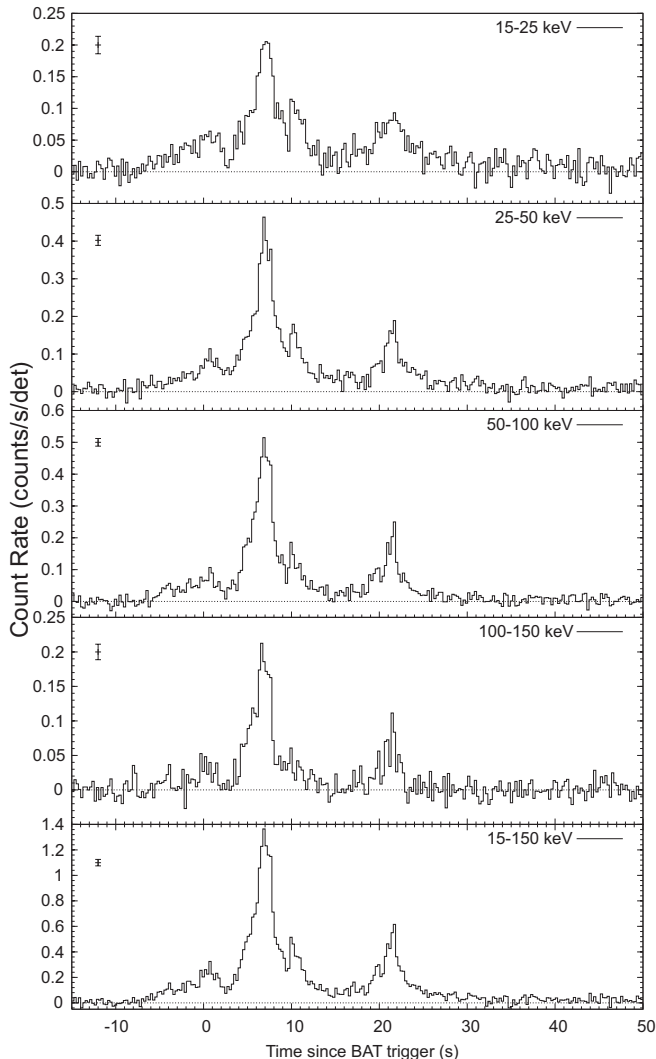


FIG. 1.—: From top to bottom: the BAT light curve of GRB 061126 during the main activity period in 15-25 keV, 25-50 keV, 50-100 keV, 100-150 keV energy bands and the sum (15-150 keV) in the bottom panel, respectively. Typical error bars are shown on the top left of each panel.

of statistically significant fluctuations around the best-fitting power law. A similar flux variability was observed also in other X-ray afterglows, such as for GRB 060124 (Romano et al. 2006). In order to investigate the possibility of a hidden X-ray break (Curran et al. 2008), fits with a broken or a smoothly broken power-law were performed, but they did not give a significant statistical improvement with respect to the simple power-law fit. Since the fit with a broken power law gives a slightly lower value of $\chi^2/\text{dof} = 193.7/97$, we performed F-test which showed that there is 33% probability that this improvement is due to a chance. Therefore, we conclude that there is no evidence for a break in the X-ray light curve up to $T_0 + 1 \times 10^6$ s.

The three XRT spectra (from WT, first PC and later PC sequence) were fitted separately using a power-law with a two component absorption, the first fixed at the Galactic value of $N_{\text{H}}^{\text{Gal}} = 1.03 \times 10^{21} \text{ cm}^{-2}$ (Kalberla et al. 2005), the second taking into account the intrinsic absorption, left free to vary. No substantial spectral evolution was found. Therefore, a simultaneous fit of the

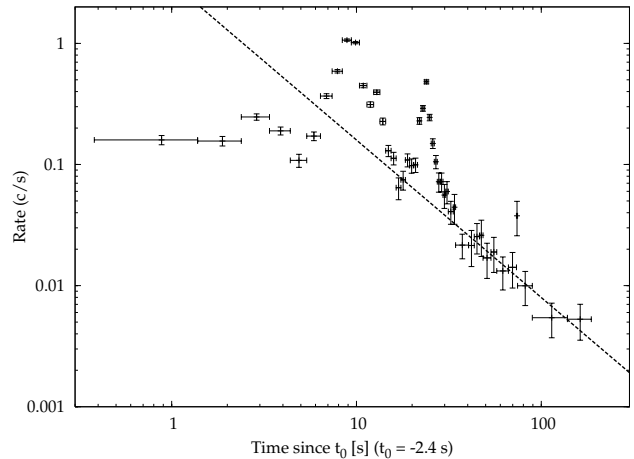


FIG. 2.—: The BAT 15-150 keV light curve with a logarithmic scale. After the second main peak the gamma tail is evident. The dashed line shows the power-law fit with $\alpha_\gamma = 1.3$.

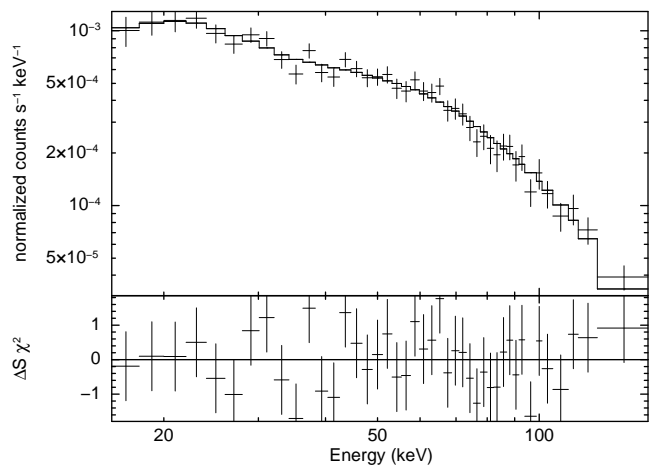


FIG. 3.—: The BAT total spectrum from $T_0 - 10$ s to $T_0 + 200$ s and the fit with the Band function and parameters $\alpha_B = -1.05 \pm 0.17$, $\beta_B = -2.3$ (fixed) and $E_p = 197_{-52}^{+173}$ keV.

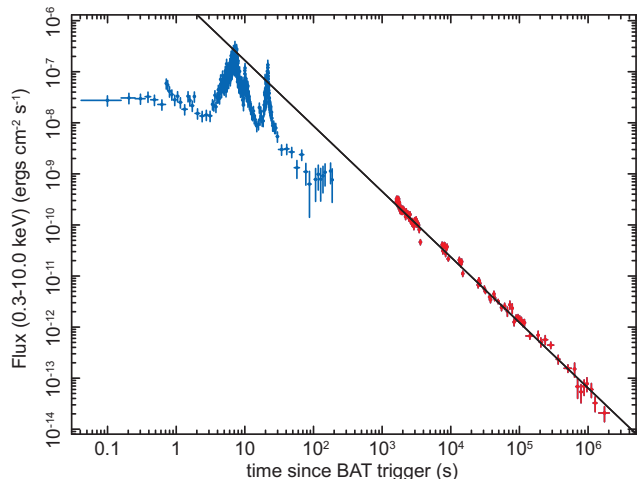


FIG. 4.—: Red: XRT light curve of GRB 061126 in 0.3 – 10 keV energy band, showing a single power-law decay with small fluctuations evident throughout. The best fit power-law index is $\alpha_X = 1.290 \pm 0.008$. Blue: BAT light curve is shown for comparison.

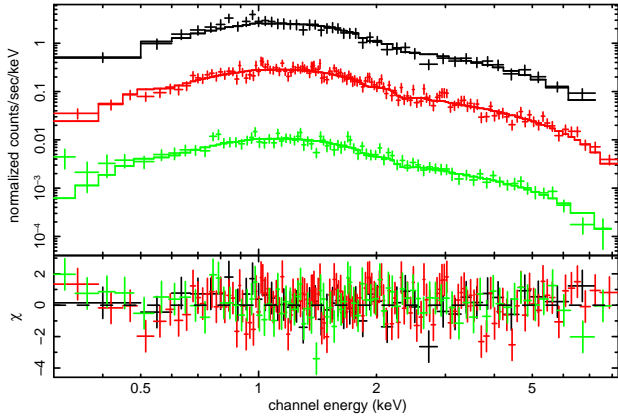


FIG. 5.— Spectral fit of XRT data for GRB 061126. Black: data and best fit for the first sequence WT mode; red: data and best fit for the first sequence PC mode (pile-up corrected); green: data and best fit for sequences 2 to 7 PC mode.

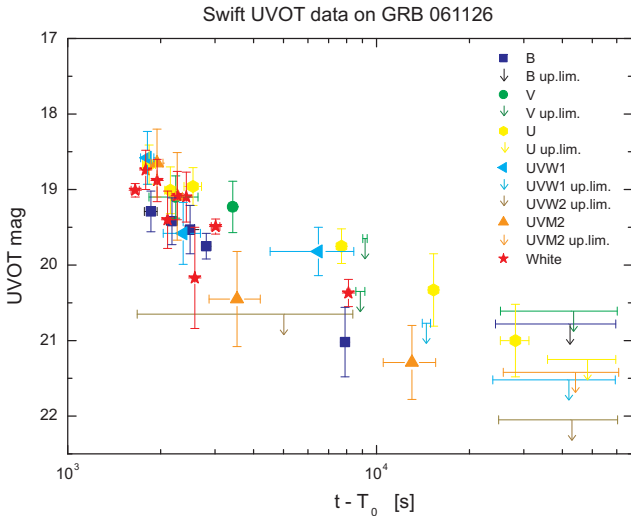


FIG. 6.— *Swift* UVOT observations of GRB 061126 afterglow in *B*, *V*, *U*, *UVW1*, *UVW2*, *UVM2* and White filters. Symbols show detections and arrows upper limits in given filter. Data shown in this plot are not corrected for galactic extinction.

three spectra was performed in order to improve the significance of the fit parameters (see Figure 5). The best fit gives a power-law index $\Gamma = 1.88 \pm 0.03$, and an intrinsic absorbing column density $N_{\text{H}} = 6.1 \pm 0.5 \times 10^{21} \text{ cm}^{-2}$.

3.3. The UV/Optical Afterglow

UVOT data are shown in Figure 6. The late start of the UVOT observations (at $T_0 + 26$ min) and the faintness of the afterglow at this time resulted in large uncertainties on the measured magnitudes. We therefore did not attempt to fit the UVOT light curves separately. From the detection of the optical counterpart in White, *V*, *B*, *U*, *UVW1* and *UVM2* filters, a photometric upper limit of the redshift of GRB 061126 could be estimated to be $z \lesssim 1.5$ (Sbarufatti et al. 2006b), which is in agreement with $z = 1.158$ estimated spectroscopically by Perley et al. (2008). UVOT data in *B* and *V* bands were re-calibrated and combined with the ground-based observations.

The ground-based optical observations are summarized in Table 1. Light curves of the optical afterglow of GRB 061126 in *BVRi'* bands are plotted in Figure 7. They show a power law decay with the steep-to-shallow transition between $T_0 + 700$ s and $T_0 + 800$ s, which is apparent in all filters. The light curves in all four filters were fitted with the same broken power-law, using all data points. The resulting χ^2/dof was high due to fluctuations in the time interval between $T_0 + 6 \times 10^3$ s to $T_0 + 2 \times 10^4$ s. Assuming a systematic error of 0.05 mag and 0.1 mag (added in quadrature) significantly improves the fit, giving broken power law parameters: $\alpha_1 = 1.48 \pm 0.06$, $\alpha_2 = 0.88 \pm 0.03$ and $t_{\text{flat}} = T_0 + (798 \pm 53)$ s with $\chi^2/\text{dof} = 278/133$ and $\chi^2/\text{dof} = 166/133$, respectively. The bottom panel of Figure 7 shows the residuals with respect to the fit, where some additional variability is still evident.

As discussed in the literature, the flattening of the optical light curve suggests a reverse shock origin for the early steep decay. Theoretical models (Kobayashi & Zhang 2003; Zhang et al. 2003; Kobayashi 2000) predict that while the reverse shock component decays with $t^{-\alpha_r}$, the forward shock emission initially rises as $\propto t^{0.5}$, reaches the peak at t_p when the typical frequency crosses the observation band, and decays afterwards with $t^{-\alpha_f}$. The total flux is then a sum of both components. At earlier times, the reverse shock emission dominates the optical band, and masks the forward shock peak. The superposition of two simple power law components is used to fit the observational data. The best fitting temporal indices are: $\alpha_r = 1.69 \pm 0.09$ and $\alpha_f = 0.78 \pm 0.04$. The quality of the fit, as indicated by $\chi^2/\text{dof} = 160/77$, does not appear to be very robust, but we believe this reflects the presence of additional fluctuations superimposed on the underlying light curve, as discussed earlier; overall, a reverse-shock, forward-shock scenario provides an adequate explanation for the underlying light curve shape. In §3.4, we develop this further by considering the effect of the late-time behavior and properly accounting for the contribution of host galaxy.

3.4. The Late-Time Afterglow and a Possible Break

From Figure 7 it is evident that there is no sign of the steepening of the optical light curve up to $T_0 + 1.3 \times 10^5$ s. We can therefore set a firm lower limit to the time of the possible late-time break to be $t_{\text{late-break}} > T_0 + 1.3 \times 10^5$ s.

Later data points obtained by the INT and Gemini North at $\sim T_0 + 3 \times 10^5$ s in *r'* and *i'* bands (which were excluded from our earlier fits) lie 3.4 and 5.0 σ below the best fit curves. This discrepancy could be due to the fluctuating nature of the afterglow or indicate the presence of late time steepening. To further investigate the latter possibility, we considered the last optical data point (Gemini North), at $T_0 + 1.3 \times 10^6$ s. This point seems to agree well with our fits, however, the Gemini image shows that the OT was already faint compared to the host galaxy. Unfortunately, it is not possible to reliably separate the contributions of the afterglow and the host galaxy to the measured magnitude. Neverthe-

³ Throughout this paper subscripts *r* and *f* indicate reverse and forward shocks, respectively.

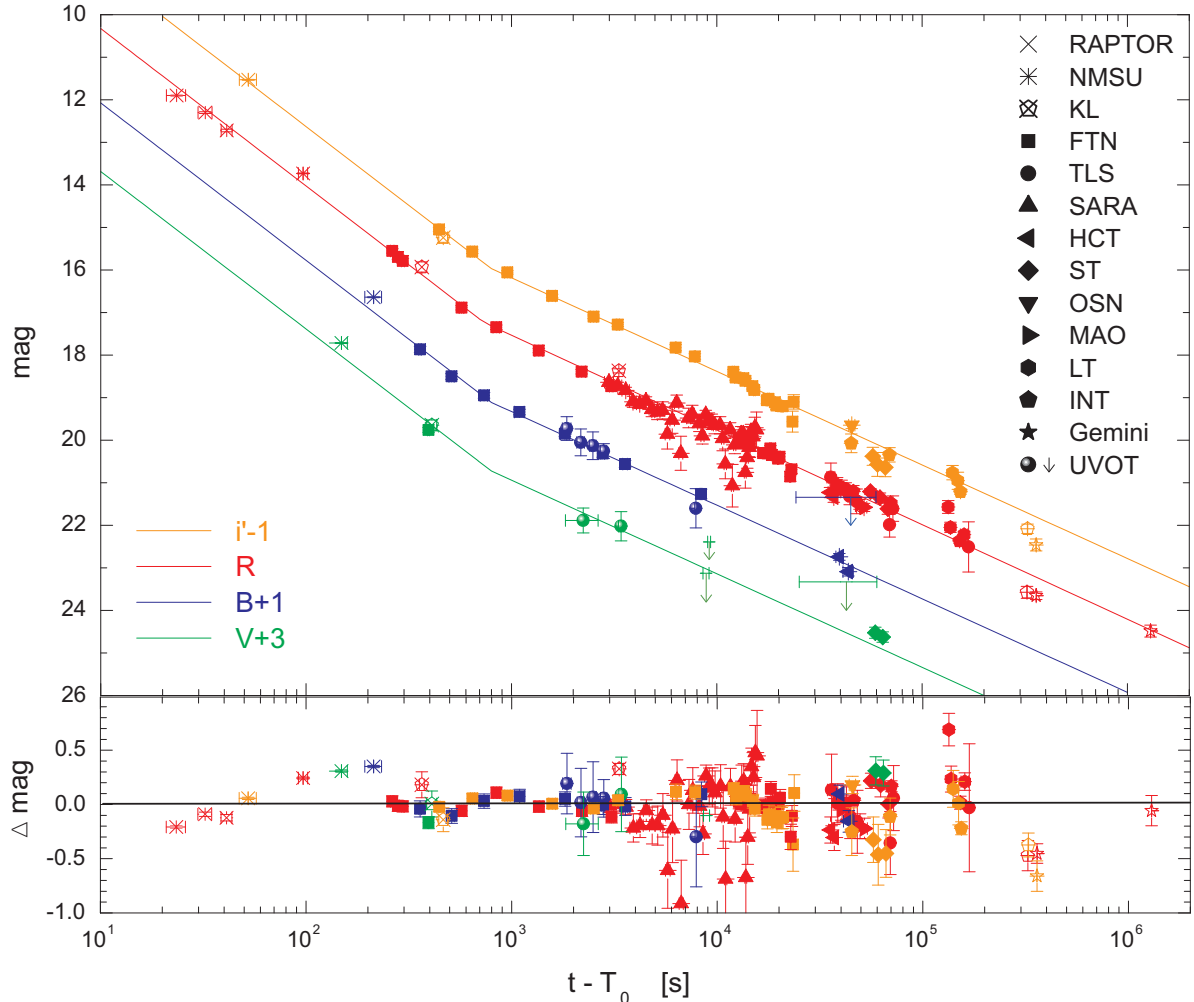


FIG. 7.— Light curves of optical afterglow of GRB 061126 in B , V , R and i' bands (r' , I data points are reported here in R , i' using Smith et al. (2002) filter transformations). Fit with a broken power law gives $\alpha_1 = 1.48 \pm 0.06$, $\alpha_2 = 0.88 \pm 0.03$ and $t_{\text{flat}} = T_0 + (798 \pm 53)$ s. Open symbols show data points which were excluded from the fit; arrows mark upper limits.

less, we can conclude that, taking into account the host galaxy contribution, the afterglow is fainter than what is expected in the absence of a late-time break. It is therefore likely that there was a steepening of the light curve before $t_{\text{late-break}} < T_0 + 1.3 \times 10^6$ s.

To further constrain the time of the possible late time break, we considered two scenarios for the last Gemini North point: (i) it represents the magnitude of the host galaxy only, or (ii) the magnitude of the host galaxy and afterglow are comparable at this time. We corrected the afterglow R -band light curve for the host contribution and repeated the above reverse-and-forward shock fit, while allowing the forward component to have a late time break. In both cases the best fit parameters α_r and α_f agree with previously derived values, while for the late time break we obtain: $t_{\text{late-break}} = T_0 + (1.31 \pm 0.2) \times 10^5$ s in both cases, and the decay index after the break $\alpha_{f,2} = 1.98 \pm 0.15$ and $\alpha_{f,2} = 1.38 \pm 0.09$ for cases (i) and (ii) respectively. The result for the case (i) is shown in Figure 8. Case (i) is favoured by Perley et al. (2008) measurement of the host galaxy magnitude $R = 24.10 \pm 0.11$ at $T_0 + 53$ days. This is brighter than our Gemini North data point at $T_0 + 15$ days (discrepancy is presumably due

to larger aperture used by Perley et al. 2008), implying that the latter is predominantly host.

From the updated Ghirlanda correlation, i.e. eq. (5) in Nava et al. (2006)⁴, we derive $E_\gamma = 7_{-3}^{+13} \times 10^{50}$ erg (taking into account the dispersion of the correlation), $\theta = 7.9_{-2.0}^{+9.3}$ and $t_{\text{jet-break}} = T_0 + 3.3_{-2.0}^{+23.1}$ days (assuming $n = 3$, $\eta = 0.2$). This value is consistent with our conservative estimate above: $1.5 \text{ days} < t_{\text{late-break}} - T_0 < 15 \text{ days}$ and with our value of $t_{\text{late-break}} = T_0 + (1.52 \pm 0.23)$ days, obtained by the fits. Nevertheless, the interpretation of this break as due to collimation is questionable, because there is no evidence of a simultaneous break in the X-rays (for more examples and discussion on optical/X-ray breaks see Willingale et al. (2007) and Liang et al. (2008)). A jet break visible only in the optical band is allowed if the X-ray emission originates from a different emission process or an emitting region that is physically distinct from that responsible for the optical radiation.

⁴ The value of 2.72 in eq. (5) in Nava et al. (2006) should be replaced with 3.72. Private communication, L. Nava.

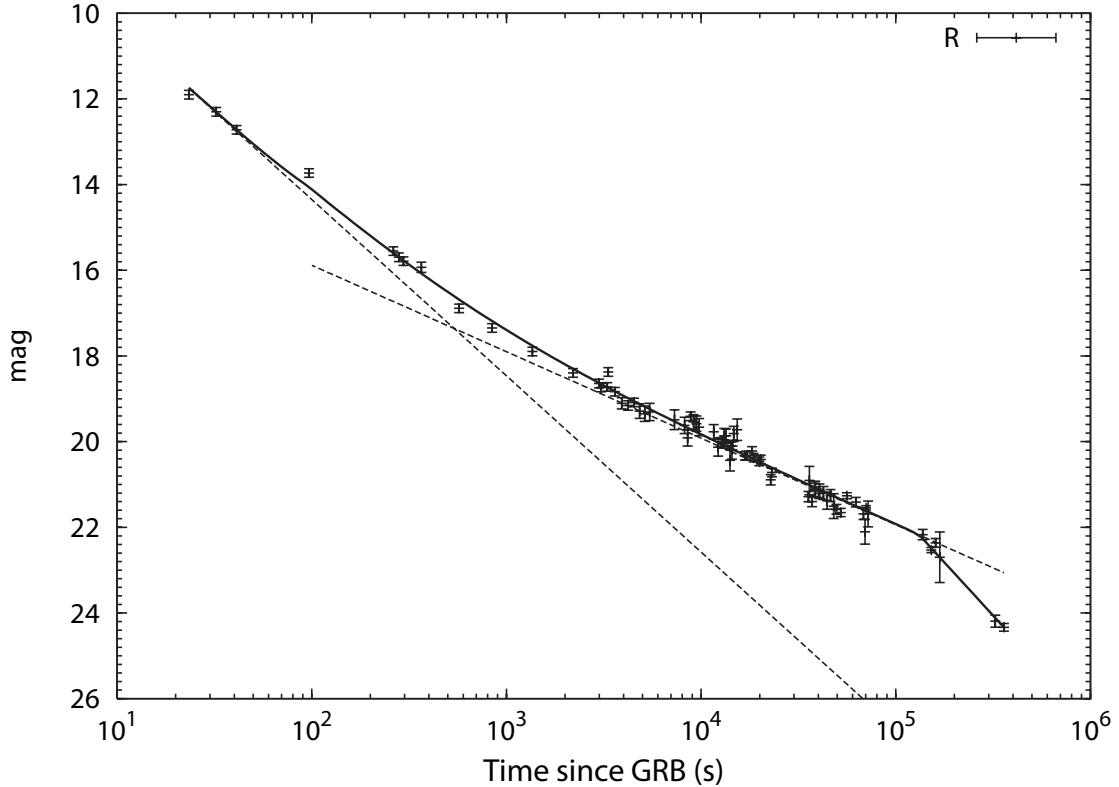


FIG. 8.—: Optical afterglow of GRB 061126 in R band (corrected for host galaxy contribution, case (i), see text) and the fit with two components: reverse shock and forward shock emission giving the best fitting parameters: $\alpha_r = 1.69 \pm 0.09$ and $\alpha_f = 0.78 \pm 0.04$. At late time we allow the forward shock component to have a break: the best fit gives $\alpha_{f,2} = 1.98 \pm 0.15$ and time of the break $t_{\text{late-break}} = (1.31 \pm 0.2) \times 10^5$ s.

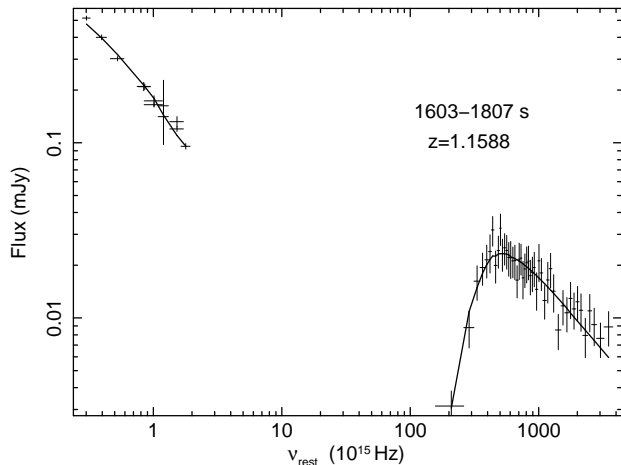


FIG. 9.—: SED after the first optical break when the light curves become shallower; at $T_0 + (1600 - 1800)$ s. Broken power-law fit gives $\nu_{\text{br}} = (4.8 \pm 1.8) \times 10^{17}$ Hz, $\beta_X = 0.88 \pm 0.03$, $\beta_O = \beta_X - 0.5 = 0.38 \pm 0.03$, $A_V = 0.38 \pm 0.03$ mag, $N_{\text{H}} = (8.8 \pm 1.2) \times 10^{21}$ cm $^{-2}$ and $\chi^2/\text{dof} = 58/53$

3.5. Spectral Energy Distributions

To further quantify the multiwavelength properties of this burst, spectral energy distributions (SEDs) at different epochs were constructed. Optical data points at particular epochs were calculated using the interpolation with the best broken power law fit derived in §3.3. SEDs are presented in the GRB rest frame assuming redshift $z = 1.1588$. In all fitting procedures we applied the

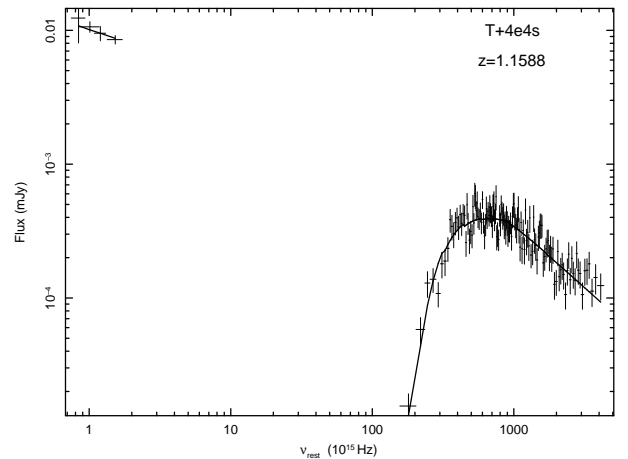


FIG. 10.—: Late time SED; at $T_0 + 4 \times 10^4$ s. Broken power-law fit gives $\nu_{\text{br}} = (9.3 \pm 1.5) \times 10^{17}$ Hz, $\beta_X = 0.98 \pm 0.02$, $\beta_O = \beta_X - 0.5 = 0.48 \pm 0.02$, $A_V < 0.13$ mag, $N_{\text{H}} = (9.2 \pm 0.8) \times 10^{21}$ cm $^{-2}$ and $\chi^2/\text{dof} = 152/133$

Small Magellanic Cloud (SMC) extinction profile (Pei 1992) and resulting A_V is the host galaxy, rest frame extinction.

3.5.1. Comparison of optical and X-ray emission at $T_0 + 50$ s and at $T_0 + 395$ s

Although the optical to X-ray SED at early time is useful for diagnosing the magnetization of a fireball, there are no early XRT observations. We therefore estimate the X-ray emission at early time from a simple back-

extrapolation of the monotonic decay α_X observed at later time. This comparison is made at two different epochs before the flattening in the optical light curve, i.e. at $T_0 + 50$ s and at $T_0 + 395$ s. We made use of the *Swift* XRT data and ground based optical data obtained by the FTN. At both epochs we obtain acceptable fits with a broken power law with: $\beta_O = \beta_X - 0.5 \approx 0.4 - 0.5$, $\nu_{br} \approx (2.4 - 5.8) \times 10^{17}$ Hz and $A_V = 0.3 - 0.55$ mag.

In the case of a strongly magnetized fireball, an excess of optical emission is predicted; no conclusive evidence for such an excess is detected in GRB061126. Nevertheless, the lack of an excess is not strongly constrained by this comparison, because even if an excess were present, the data could be equally well fitted with a different broken power law with a lower ν_{br} . The use of an SED to determine the magnetization of the fireball is therefore weak in this case and we introduce a more robust parameter to investigate magnetization in §4.1.

3.5.2. SED at $T_0 + (1600 - 1800)$ s

Figure 9 shows the SED constructed at $T_0 + (1600 - 1800)$ s, shortly after the optical light curves become shallower, and when the *Swift* XRT observations began. We include the FTN and Perley et al. (2008) data. A single power law does not give an acceptable fit. However, fitting the SED with a broken power law, assuming $\beta_O = \beta_X - 0.5$, gives an acceptable fit ($\chi^2/\text{dof} = 58/53$) with the break frequency between the optical and X-ray bands. Best fit parameters are: $\nu_{br} = (4.8 \pm 1.8) \times 10^{17}$ Hz, $\beta_X = 0.88 \pm 0.03$, $\beta_O = 0.38 \pm 0.03$, $A_V = 0.38 \pm 0.03$ mag, and $N_H = (8.8 \pm 1.2) \times 10^{21}$ cm $^{-2}$. The best fit to the SED is shown in Figure 9. Our result is not in agreement with results by Perley et al. (2008), who find $A_V = 1$ mag and $A_V \approx 0.6 - 0.9$ mag in their broadband fits. Nevertheless, general conclusion, that the relative optical faintness (when compared to X-ray flux) is not due to absorption, is the same.

3.5.3. SED at $T_0 + 4 \times 10^4$ s

The late time SED at $T_0 + 4 \times 10^4$ s includes the *Swift* XRT and ground-based optical data in B (by HCT), V (by ST), R (by TLS, HCT, MAO and INT) and i' (by S. Nevada and INT) filters. The SED is shown in Figure 10, which also shows the best fit with a broken power-law with parameters: $\nu_{br} = (9.3 \pm 1.5) \times 10^{17}$ Hz, $\beta_X = 0.98 \pm 0.02$, $\beta_O = \beta_X - 0.5 = 0.48 \pm 0.02$, $A_V < 0.13$ mag, $N_H = (9.2 \pm 0.8) \times 10^{21}$ cm $^{-2}$ and $\chi^2/\text{dof} = 152/133$.

Although the uncertainty on the break frequency ν_{br} derived from the fits to the SEDs at different epochs is relatively large, there is a suggestion that ν_{br} is increasing with time. We discuss possible reasons for this in §4.2.

3.6. Dark, gray or neither?

The time of the last SED, $T_0 + 11$ h, is the time at which Jakobsson et al. (2004) compare the X-ray and optical fluxes of GRBs and define the slope of the spectral energy distribution between the optical and the X-ray band $\beta_{OX} = 0.5$ as dividing optically bright from optically dark bursts. In the case of GRB 061126, at early time β_{OX} is less than this value (as also noted by Perley et al. 2008): our data yield $\beta_{OX} = 0.29 \pm 0.04$ at $T_0 + 2000$ s, which is in slight excess of $\beta_{OX} = 0.23$, derived by Perley

et al. (2008). GRB 061126 could therefore be classified as a dark burst, in spite of the fact that at this early time, it is one of the optically brightest bursts detected (see for example Figure 1 in Kann et al. 2007). However, as the afterglow is fading more slowly in the optical than in X-rays, β_{OX} is increasing with time. At $T_0 + 11$ h we find that $\beta_{OX} = 0.53 \pm 0.02$, i.e. on the “edge” of being a dark burst. This burst is clearly one of those for which the Jakobsson classification must be considered as a function of time and for which a simple extrapolation to/from $T_0 + 11$ h is inadequate (for other possible cases see Melandri et al. 2008).

Nevertheless, observations at early time give a stringent test, i.e. a value of β_{OX} below the theoretical limit of 0.5 implies that we can not explain it in the standard fireball model.

4. DISCUSSION

4.1. Optical Emission

The early optical behavior of GRB 061126 resembles the optical light curves of GRB 990123 (Akerlof et al. 1999; Nakar & Piran 2005), GRB 021211 (Fox et al. 2003; Pandey et al. 2003) and GRB 060117 (Jelinek et al. 2006). We note particular similarity with the optical afterglow of GRB 021211, not only in similar t_{flat} , α_1 and α_2 , but also in cosmological redshift. As discussed in these previous cases, the flattening behavior of light curves can be interpreted with a reverse and forward shock scenario. The light curve of GRB 061126 is composed of two segments: an initial steep decline followed by a shallower decay with the typical decay index of afterglow $\alpha \sim 1$. While this typical, shallower decay is due to the forward shock (with $\alpha_f \approx 0.8$), the most likely explanation for the early optical emission is that it is dominated by short-lived emission from a reverse shock (Mészáros and Rees 1997; Sari & Piran 1999) (with $\alpha_r \approx 1.7$). The color change reported by Perley et al. (2008) also implies the presence of different emission components.

The emission components of forward and reverse shocks were studied in a unified manner by Kobayashi & Zhang (2003) and Zhang et al. (2003). The optical light curve of GRB 061126 (and those of GRB 990123 and GRB 021211) is well described by the flattening type light curve in Zhang et al. (2003). The evolution of reverse shocks is classified into two cases (Sari & Piran 1995) depending on the initial Lorentz factor of a fireball shell Γ . The critical value is:

$$\Gamma_c = [3(1+z)^3 E / 32\pi n m_p c^5 T^3]^{1/8},$$

where E , T , n , z , m_p are the explosion energy, the duration of prompt emission, the ambient matter density, the redshift and the mass of proton, respectively.

If $\Gamma > \Gamma_c$, the reverse shock becomes relativistic in the frame of unshocked shell material whilst crossing the shell, and drastically decelerates the shell (thick shell case). If $\Gamma \lesssim \Gamma_c$, the reverse shock cannot decelerate the shell effectively (thin shell case). Since the optical afterglow is already fading immediately after the prompt gamma-ray emission, the initial Lorentz factor should be comparable to or larger than the critical value (Sari 1997). Alternatively, if $\Gamma \gg \Gamma_c$, the reverse shock emission should initially drop sharply with $\alpha \sim 3$, as

a rarefaction wave quickly transfers the shell's internal energy to the ambient matter (Kobayashi & Sari 2000; Kobayashi & Zhang 2007). Therefore, in the case of GRB 061126, the initial Lorentz factor should be close to the critical value,

$$\Gamma \sim \Gamma_c = 260 n^{-\frac{1}{8}} \left(\frac{1+z}{2.16} \right)^{\frac{3}{8}} \left(\frac{T}{30 \text{ sec}} \right)^{-\frac{3}{8}} \left(\frac{E}{7.4 \times 10^{52} \text{ erg}} \right)^{\frac{1}{8}}. \quad (1)$$

For $\Gamma \sim \Gamma_c$, the reverse shock does not heat the shell well. The thin shell model should be applicable to characterize the reverse shock light curve. After the shock crossing $t > T$, reverse shock light curves at frequencies $\nu_{m,r} < \nu < \nu_{c,r}$ behave as $F_\nu \propto t^{-(3p+1)/4}$, where $\nu_{m,r}$ and $\nu_{c,r}$ are the typical and cooling frequencies of the reverse shock emission, p is the electron spectral index, and a simple approximation form is employed for the decay index (Zhang et al. 2003). Light curves at frequencies $\nu < \nu_{m,r}$ are shallower as $F_\nu \propto t^{-16/35}$, and there is essentially no emission above $\nu_{c,r}$ (Kobayashi 2000). The observed decay index $\alpha_r = 1.69 \pm 0.09$ suggests $\nu_{m,r} < \nu < \nu_{c,r}$ during the steep decay phase and electron distribution index $p \sim 1.9$. As also observed in other bursts, there is a bump feature in the optical light curve around the break $t \sim t_{\text{flat}}$ (Perley et al. 2008). A density variation in the ambient medium is often discussed as the origin of bump features (e.g. Lazzati et al. 2002; Guidorzi et al. 2005; Mundell et al. 2007a). If the bump is subtracted from the light curve, the values of α and p could be larger.

At the shock crossing time $t \sim T$, the spectral characteristics of the forward and reverse shock emission are related by the following simple formulae (Zhang et al. 2003),

$$\frac{\nu_{m,r}}{\nu_{m,f}} \sim \Gamma^{-2} R_B^{1/2}, \quad \frac{\nu_{c,r}}{\nu_{c,f}} \sim R_B^{-3/2}, \quad \frac{F_{\text{max},r}}{F_{\text{max},f}} \sim \Gamma R_B^{1/2}, \quad (2)$$

where $F_{\text{max},r}$ and $F_{\text{max},f}$ are the peak flux of the reverse and forward shock emission. We have assumed that p and the electron equipartition parameter ϵ_e are the same for both the forward and reverse shock regions, but with different magnetic equipartition parameter ϵ_B as parameterized by the magnetic energy ratio $R_B = \epsilon_{B,r}/\epsilon_{B,f}$. Note that the definition of the magnetization correction factor is different from that in Zhang et al. (2003). The reason we introduce the R_B parameter is that a fireball may be endowed with primordial magnetic fields at the central engine, so that in principle R_B could be larger than unity. As we will discuss in §4.2, the optical light curve (before and after the break t_{flat}) is consistent with the assumption that p is the same in the two shock regions.

Assuming no or moderate primordial magnetization in the fireball, we obtain a relation $\nu_{m,r} < \nu_{m,f} < \nu_{c,r} \leq \nu_{c,f}$ at the shock crossing time. Since $\nu_{m,r} < \nu_{\text{opt}} < \nu_{c,r}$ should hold during the steep decay phase, the optical band should be at $\nu_{m,r} < \nu_{\text{opt}} < \nu_{m,f}$ or $\nu_{m,f} < \nu_{\text{opt}} < \nu_{c,r}$ at $t = T$. In the former case, the forward shock emission should peak at $t = t_p$ when the typical frequency $\nu_{m,f}$ goes through the optical band. Using $\nu_{m,f}(t_p) = \nu_{\text{opt}}$ and a scaling $\nu_{m,f} \propto t^{-3/2}$, one

finds the peak time ratio as

$$R_t \equiv t_p/T = (\nu_{m,f}(T)/\nu_{\text{opt}})^{2/3}. \quad (3)$$

Following a similar discussion in Zhang et al. (2003), the peak flux ratio is⁵

$$R_F \equiv F_{p,r}/F_{p,f} = F_{\text{max},r}(\nu_{\text{opt}}/\nu_{m,r})^{-(p-1)/2}/F_{\text{max},f} \quad (4) \\ = \Gamma^{-(4\alpha_r-7)/3} R_B^{(2\alpha_r+1)/6} R_t^{\alpha_r-1}, \quad (5)$$

where $\alpha_r = (3p+1)/4$ is the decay index of reverse shock emission, and we have used equations (2) and (3). Modifying equation (5), the magnetic energy ratio is given by

$$R_B = \left(\frac{R_F \Gamma^{(4\alpha_r-7)/3}}{R_t^{\alpha_r-1}} \right)^{6/(2\alpha_r+1)}. \quad (6)$$

In the latter case $\nu_{m,f} < \nu_{\text{opt}} < \nu_{c,r}$, the forward shock emission also peaks at $t = T$, and it follows that $R_t = 1$. It is possible to show that equation (6) is still valid.

This event is a marginal case with $\Gamma \sim \Gamma_c$, and the reverse shock emission should peak around the end of the prompt gamma-ray emission at $t \sim 30$ s. Unfortunately the forward shock peak t_p was not caught (it means that $t_p \lesssim t_{\text{flat}} \sim 800$ s), because the reverse shock emission dominated at early times. First we consider the case with the upper limit $t_p = t_{\text{flat}}$, and estimate R_B . The peak time ratio is $R_t \sim 27$. Since the optical light curve flattens at $t_{\text{flat}} (\sim t_p)$, the reverse shock and forward shock components are comparable at that time: $F_r(t_p) = F_{p,r}(t_p/T)^{-\alpha_r} \sim F_{p,f}$, and it follows that the peak flux ratio can be written as $R_F \sim R_t^{\alpha_r}$. Substituting this relation into equation (6) we obtain

$$R_B \sim \left(R_t^3 \Gamma^{(4\alpha_r-7)} \right)^{2/(2\alpha_r+1)} \sim 50 \quad \text{for } \alpha_r = 1.69, \quad (7)$$

where ambient matter density $n = 1$ proton/cm³ is assumed, but the result is insensitive to n as $R_B \propto n^{0.01}$ for $\alpha_r = 1.69$. If the forward shock emission reaches the maximum earlier $t_p < t_{\text{flat}}$, the value of R_B might be different. To evaluate how R_B depends on t_p , we refer to scalings: $R_t \propto t_p$ and $R_F \propto F_{p,f}^{-1} \propto t_p^{\alpha_f}$, where we took into account that the peak of the forward shock emission should be on the power law line with α_f . Using these scalings, one finds that the dependence is weak⁶: $R_B \propto t_p^{6(1-\alpha_r+\alpha_f)/(1+2\alpha_r)} \propto t_p^{0.12}$ for $(\alpha_r, \alpha_f) = (1.69, 0.78)$. In the earliest case $t_p \sim 30$ s, we obtain $R_B \sim 34$. These results imply that magnetic energy density in a fireball is much larger than in the forward shock. Nevertheless, as a small value of $\epsilon_{B,f} \sim 10^{-4} - 10^{-2}$ is usually inferred from afterglow modeling (e.g. Panaitescu & Kumar 2002), the above values of R_B suggest that $\epsilon_{B,r} \ll 1$ and the energy in the fireball is still likely to take the form of kinetic energy (a baryonic fireball) rather than Poynting flux.

⁵ This ratio R_F differs from $F_{\text{max},r}/F_{\text{max},f}$ defined in eq. 2: F_{max} is a peak flux in the spectral domain at a given time, while F_p is a peak flux in the time domain at a given frequency.

⁶ If the decay indices of the forward-shock and reverse-shock emission exactly satisfy the theoretical values: $\alpha_f = 3(p-1)/4$ and $\alpha_r = (3p+1)/4$, a relation $\alpha_r - \alpha_f = 1$ should hold, and R_B does not depend on t_p .

Recently the Liverpool Telescope obtained an early-time estimate of optical polarization of a GRB afterglow shortly after the burst (Mundell et al. 2007b). Polarization observations of an afterglow with a flattening light curve or at the time of a reverse shock peak would provide additional constraints on the presence of magnetized fireballs.

4.2. X-ray Emission

The X-ray afterglow was observed from $\sim T_0 + 26$ min to $T_0 + 20$ days by *Swift* XRT. The X-ray light curve fades as a single power law with a decay index $\alpha_X = 1.290 \pm 0.008$. Since this is steeper than the optical light curve $\alpha_f \sim 0.8$ over the same period, the X-ray band should be in a different spectral domain than the optical, therefore: $\nu_{m,f} < \nu_{\text{opt}} < \nu_{c,f} < \nu_X$. The observed X-ray spectral index $\beta_X = 0.94 \pm 0.05$ corresponds to $p = 2\beta_X \sim 2.0$. The optical emission from the reverse shock and forward shock should decay as $\alpha_r = (3p + 1)/4 = 1.75$ and $\alpha_f = 3(p - 1)/4 = 0.75$, respectively. These are in good agreement with the observed $\alpha_r = 1.69 \pm 0.09$ and $\alpha_f = 0.78 \pm 0.04$. As we have discussed in the previous section, the bump feature in the early optical light curve might make the observed α_r smaller and the observed α_f larger.

The observed emission in X-rays ($\alpha_X = 1.29$) decays faster than that expected from the X-ray spectral index $\alpha_X = (3p - 2)/4 = 1.0$. This discrepancy might be due to the radiative loss. If the energy distribution of electrons is flat $p \sim 2$, each decade in the electron distribution contains the same amount of energy, and if $p < 2$, high energy electrons have most of the total electron energy. Even in the slow cooling regime $\nu_m < \nu_c$, the radiative loss might make the decay steeper $\Delta\alpha \sim \epsilon_e$ (Sari 1997). However, the radiation loss affects the optical emission also, and the expected (steeper) optical index is not consistent with the observations. More general discussion on the time dependent parameters can be given as follows. The ratio of X-ray to optical flux depends on parameters as

$$F_X/F_{\text{opt}} \propto \nu_{c,f}^{1/2} \propto \epsilon_{B,f}^{-3/4} E^{-1/4} n^{-1/2} t^{-1/4} \quad (8)$$

where we have assumed the standard synchrotron spectrum ($\nu_{m,f} < \nu_{\text{opt}} < \nu_{c,f} < \nu_X$) and an adiabatic evolution of the blast wave. If the parameters are slowly changing in time (e.g. radiation loss, late-time energy injection, time dependent microscopic parameters or a gradient in the ambient density), the difference of the decay indexes in the two bands could be larger than the standard value $\Delta\alpha = \alpha_X - \alpha_O = 1/4$. The observed difference $\Delta\alpha = 0.51$ requires that the parameters should increase with time. This is a somewhat unphysical condition, and causes a large discrepancy between the theoretical and observed optical decay indices, because the optical flux is sensitive to the parameters as $F_{\text{opt}} \propto \epsilon_e^{p-1} \epsilon_{B,f}^{(p+1)/4} E^{(p+3)/4} n^{1/2} t^{-3(p-1)/4}$. Inverse Compton scattering can, in principle, affect the cooling frequency $\nu_{c,f}$, and a correction factor to $\nu_{c,f}$ is time-dependent during the slow cooling phase. However, the presence of strong Inverse Compton cooling will make the difference $\Delta\alpha$ even smaller (Sari & Esin 2001).

An alternative possibility for the production of the X-ray afterglow is a continued activity of the central engine

(e.g. late prompt emission, Ghisellini et al. 2007; Fan et al. 2008) or a two-component jet (Racusin et al. (2008) and the references therein). The optical light curve shows evidence of a late time break which is consistent with the value derived from the Ghirlanda relation. The lack of a simultaneous (jet) break in the X-ray light curve might indicate that the X-rays originate from a different emission site. Another indication is the low value of β_{OX} at early times (see §3.6), which might suggest the enhancement of the X-ray flux due to the additional emission (Perley et al. 2008; Melandri et al. 2008). If the additional emission (e.g. late-time prompt emission or narrow jet emission in the two-component jet model) masks the forward shock emission in X-ray band, the decay rate is determined by the process related to the additional component. In principle the decay rate could be faster than that implied by the fireball model until the forward shock emission is eventually unmasked. To interpret the chromatic afterglow of GRB 080319B, Racusin et al. (2008) suggest a two-component jet model in which the additional component (emission from a spreading narrow jet) decays faster than the underlying component (wide jet emission) responsible for the optical component. In the case of GRB 061126, the faster decay in X-ray could be explained if the electron distribution index p is not universal and larger in the narrow jet, though we need to explain what causes the difference of p in the two jets. Furthermore, the X-ray (narrow-jet emission) light curve does not show a jet break before $T_0 + 10^6$ s, while the optical (wide-jet emission) light curve shows a possible steepening at $t < T_0 + 3 \times 10^5$ s. The two-component jet model might be disfavored to explain GRB 061126. As Perley et al. (2008) have discussed, any additional component models might share a difficulty to explain how to avoid contaminating the blue end of the observed optical spectrum with emission from the low-energy tail of the additional emission (a synchrotron-like spectrum) peaking at X-ray wavelengths. This could require fine-tuning or tight constraints on the additional emission model (e.g. the self absorption frequency of the additional emission is higher than the optical band).

As we noted in §3.5, our fits suggest that ν_{br} is increasing with time. This could imply the presence of a wind environment. We have assumed a homogeneous ambient medium (ISM) in the above discussion. Even in a wind medium, the relations (2) are valid. The same relation $\nu_{m,r} < \nu_{\text{opt}} < \nu_{c,r}$ should be satisfied to explain the steep optical decay in the context of the reverse shock emission. At late times $t > t_{\text{flat}}$, if the optical and X-ray afterglows are due to the forward shock, the X-ray decay rate should be the same as or slower than the optical decay rate, because the cooling frequency $\nu_{c,f}$ moves blue-ward in the wind model. This is inconsistent with the observations. Therefore, the ISM model is favored.

One possible explanation for the increase of the break frequency would be related to the reverse shock emission component at early time. When the relation $\nu_{\text{opt}} < \nu_{c,f} < \nu_X$ is satisfied, the forward shock emission spectrum (optical to X-ray) is fitted with a broken power law. Even if reverse shock emission dominates the optical band, the spectrum could be still well fitted with a broken power law with a lower break frequency, because we observe only optical and X-ray fluxes and our sam-

plings are spares in the frequency domain. The reverse shock component decays faster than the forward shock component, and it becomes less prominent at late times. The break frequency should increase and approaches the break frequency of the forward shock at late times. This might explain the observed behavior. However, at the time the X-ray observations started and onwards, the contribution of the reverse shock to the optical emission is already negligible and could not significantly influence the break frequency. Another possibility is that of late-time prompt emission i.e. X-rays coming from an emission site other than that of the forward shock.

The gamma-ray tail is described by a power law with $\alpha_\gamma = 1.3$. The similarity of α_γ with α_X index leads to a speculation that the γ tail is due to the same forward shock and that the gamma-ray band at the early times $t > T_0 + 30$ s and the X-ray band at late times $t > T_0 + 26$ min are in the same spectral domain: $\nu_{c,f} < \nu_X, \nu_\gamma$. However, using $\alpha = 1.3$, the extrapolated value in gamma-ray band at $t = T_0 + 26$ min gives a spectral index $\beta_{X-\gamma} \sim 0.2$, which is much shallower than the observed x-ray spectrum $\beta_X \sim 1$. We therefore suspect that the same decay index $\alpha_\gamma \sim \alpha_X \sim 1.3$ happened by chance. The bright gamma-ray tail might be produced by the superposition of internal shock emission (central engine activity) or the propagation of the forward shock in a higher density ambient medium (if so, the cooling frequency should be above the gamma-ray band at $t < T_0 + 200$ s).

5. CONCLUSIONS

GRB 061126 was a long burst with intriguing optical and X-ray afterglows. The optical light curve shows a steep-to-flat transition at about 13 min after the trigger. We showed that the early, steep component can be interpreted as due to the reverse shock ($\alpha_r = 1.69 \pm 0.09$), while the later slowly fading component as coming from the forward shock ($\alpha_f = 0.78 \pm 0.04$). From the afterglow properties we deduce that $\Gamma \sim \Gamma_c \sim 260$ and estimate the magnetic energy ratio to be $R_B \sim 34 - 50$. This indicates

that the magnetic energy density in the fireball is much larger than in the forward shock at the fireball deceleration, but that the fireball is still likely to be baryonic and not Poynting flux dominated.

The standard fireball model can explain the optical decay indices before and after the flattening, i.e. α_1 and α_2 , and the X-ray spectral index β_X with a single value of electron index $p \sim 2$. However, the X-ray decay index $\alpha_X = 1.290 \pm 0.008$ deviates from the expected value $\alpha_X = 1.0$. We investigated the generalized standard fireball model with time dependent parameters (e.g. radiation loss, late time energy injection, time dependent microscopic parameters or a gradient in the ambient density), and we found that none of these modified models can explain the observed decay and spectral indices in a consistent manner. This could imply the presence of late-time prompt emission and a different origin of the X-ray afterglow, which would also be a possible explanation for the large ratio of X-ray to optical fluxes (i.e. shallow spectral index from optical to X-ray band) and for the possible chromatic jet break at $T_0 + 1.5$ days. Although there are significant fluctuations in the observed X-ray light curve, the late time internal-shock model could require a fine tuning of the central engine to explain the power-law decay.

6. ACKNOWLEDGEMENTS

AG thanks Slovenian Research Agency and Slovenian Ministry for Higher Education, Science, and Technology for financial support. C.G., V.M. and B.S. acknowledge support from ASI grant I/011/07/0. CGM acknowledges financial support from the Royal Society and Research Councils U. K. *RoboNet-1.0* was supported by PPARC and STFC. *Swift* mission is funded in the UK by STFC, in Italy by ASI, and in the USA by NASA. The Faulkes Telescopes are operated by the Las Cumbres Observatory. The Liverpool Telescope is owned and operated by Liverpool John Moores University. We thank the anonymous referee for useful comments and suggestions.

REFERENCES

- Akerlof, C. et al, 1999, *Nature*, 398, 400.
 Amati, L., 2006, *MNRAS*, 372, 233.
 Baliyan, K. S., et al. 2006, *GCN Circ.* 5864.
 Band, D. et al., 1993, *ApJ*, 413, 281.
 Bessel, M.S., 1979, *PASP*, 91, 589.
 Bloom, J. S., 2006, *GCN Circ.* 5858.
 Cardelli, J.A., Clayton, G.C., Mathis, J.S., 1989, *ApJ*, 345, 245.
 Cool, R. J. 2006, *GCN Circ.* 5985.
 Curran, P.A., van der Horst, A.J., Wijers, R.A.M.J., 2008, *MNRAS*, 386, 859.
 Della Valle, M. et al., 2003, *A&A*, 406, L33.
 Fan, Y.Z. et al., 2002, *Chin. J. Astron Astrophysics*, 2, 449.
 Fan, Y.Z., Piran, T., Wei, D.M., 2008, *AIP Conference Proceedings*, 968, 32.
 Fox, D.W. et al, 2003, *ApJ*, 568, L5.
 Fukugita, M., et al., 1996, *AJ*, 111, 1748.
 Gehrels, N., et al. 2004, *ApJ*, 611, 1005.
 Ghisellini, G., et al., 2007, *ApJ*, 658, L75.
 Gomboc, A., et al. 2006, *Il Nuovo cimento C*, 121B, Issue 10-11, 1303.
 Guidorzi, C., et al. 2005, *ApJ*, 630, L121.
 Guidorzi, C., et al. 2006, *PASP*, 118, 288.
 Holtzman, J., Harrison, T., McNamara, B., 2006, *GCN Circ.* 5894.
 Jakobsson, P., et al. 2004, *ApJ*, 617, L21.
 Jelinek, M. et al., 2006, *A&A*, 454, L119.
 Jelinek, M., et al., 2007, *astro-ph 0702197*.
 Kalberla, P.M.W., et al., 2005, *A&A*, 440, 775.
 Kann, D. A. & Malesani, D., 2006, *GCN Circ.* 5866.
 Kann, D. A. et al., 2007, *arXiv:0712.2186v1*.
 Kobayashi, S. 2000, *ApJ*, 545, 807.
 Kobayashi, S., & Sari, R. 2000, *ApJ*, 542, 819.
 Kobayashi, S., & Zhang, B. 2003, *ApJ*, 582, L75.
 Kobayashi, S., & Zhang, B. 2007, *ApJ*, 655, 973.
 Krimm et al., 2006, *GCN Circ.* 5860.
 Kumar, P. & Panaitescu, A., 2003, *MNRAS*, 346, 905.
 Landolt, A. U., 1992, *AJ*, 104, 340.
 Lazzati, D., et al. 2002, *A&A*, 396, L5.
 Li, W., et al. 2003, *ApJ*, 586, L9.
 Liang, E.W. et al., 2008, *ApJ*, 675, 528.
 Melandri, A. et al., 2008, *ApJ*, 686, ??, *arXiv:0804.0811v1*.
 Mészáros, P., 2006, *Rep. Prog. Phys.*, 69, 2259.
 Mészáros, P., & Rees, M.J. 1997, *ApJ*, 476, 232.
 Misra, K., 2006, *GCN Circ.* 5903.
 Mundell, C.G. et al. 2007a, *ApJ*, 660, 489.
 Mundell, C.G. et al. 2007b, *Science*, 315, 1822.
 Nakar, E. and Piran, T. 2005, *ApJ*, 619, L147.
 Nava, L. et al., 2006, *A&A*, 450, 471.
 Panaitescu, A. & Kumar, P., 2002, *ApJ*, 571, 779.
 Pandey, S.B. et al., 2003, *A&A*, 408, L21.
 Pei, Y.C., 1992, *ApJ*, 395, 130.
 Perley, D.A. et al., 2008, *ApJ*, 672, 449.

- Piran, T. and Fan, Y.Z. 2007, Philosophical Transactions of the Royal Society A: Mathematical, Physical and Engineering Sciences, 365, 1151.
- Pozanenko, A., et al. 2006, GCN Circ. 5902.
- Racusin, J.L. et al., 2008, arXiv:0805.1557v1.
- Rol, E., Wiersema, K., Prema, P. 2006, GCN Circ. 5876.
- Romano, P. et al., 2006, A&A, 456, 917.
- Sari, R. 1997, ApJ, 489, L37.
- Sari, R. & Esin, A., 2001, ApJ, 548, 787.
- Sari, R. & Piran, T., 1999, ApJ, 517, L109.
- Sari, R. & Piran, T., 1999, ApJ, 520, 641.
- Sbarufatti, B., et al. 2006a, GCN Circ. 5854.
- Sbarufatti, B., et al. 2006b, GCN Report-16.2.
- Schlegel, D. J., Finkbeiner, D. P., Davis, M., 1998, ApJ, 500, 525.
- Smith, J.A., et al. 2002, AJ, 123, 2121.
- Smith, R.J., et al. 2006, GCN Circ. 5857.
- Torii, K., 2006, GCN Circ. 5868.
- Updike, A. C., et al. 2006, GCN Circ. 5859.
- Vanden Berk, D. E., et al. 2006, GCN Circ. 5856.
- Vreeswijk, P.M. et al. 2002, GCN Circ. 1785.
- Wei, D.M., 2003, A&A, 402, L9.
- Williams, G. G., Milne, P.A., 2006, GCN Circ. 5869.
- Willingale, R. et al., 2007, ApJ, 662, 1093.
- Wren, J., et al. 2006, GCN Circ. 5873.
- Zhang, B., Kobayashi, S., & Mészáros, P. 2003, ApJ, 595, 950.
- Zhang, B., 2007, ChJAA, 7, 1.
- Zhang, B., et al. 2007, ApJ, 655, L25.

TABLE 1: Summary of Optical Observations of GRB 061126 with the Faulkes Telescope North (FTN), Tautenburg Schmidt telescope (TLS), SARA, Sampurnanand Telescope (ST), Himalayan Chandra Telescope (HCT), 1.5-m telescope at Observatorio de Sierra Nevada (OSN), 1.5-m telescope at Maidanak Observatory (MAO), Liverpool Telescope (LT), Isaac Newton Telescope (INT) and Gemini North. T_{start} , T_{end} and ΔT_{mean} are referred to trigger time T_0 . ΔT_{mean} is defined as $\frac{\sum_i(t_i \Delta t_i)}{\sum_i(\Delta t_i)}$, where t_i is the mid time of individual exposures and Δt_i is the exposure length.

Telescope	Filter	ΔT_{mean} (min)	Mag \pm Err	T_{start} (min)	T_{end} (min)	T_{exp} (s)
FTN	R_C	4.38	15.55 ± 0.05	4.30	4.47	10
	R_C	4.67	15.70 ± 0.05	4.59	4.76	10
	R_C	4.93	15.79 ± 0.05	4.85	5.02	10
	R_C	9.53	16.89 ± 0.05	9.28	9.78	30
	R_C	14.1	17.35 ± 0.05	13.6	14.6	60
	R_C	22.7	17.89 ± 0.05	21.7	23.7	120
	R_C	36.7	18.39 ± 0.05	35.2	38.2	180
	R_C	51.1	18.73 ± 0.06	50.1	52.1	120
	R_C	212.7	19.99 ± 0.06	210.1	215.3	300
	R_C	218.0	20.03 ± 0.06	215.4	220.6	300
	R_C	236.5	20.08 ± 0.06	233.9	239.2	300
	R_C	241.9	20.08 ± 0.06	239.3	244.5	300
	R_C	280.3	20.31 ± 0.07	277.8	283.0	300
	R_C	285.7	20.31 ± 0.07	283.1	288.3	300
	R_C	304.3	20.20 ± 0.07	301.7	306.9	300
	R_C	309.6	20.35 ± 0.08	307.0	312.2	300
	R_C	331.7	20.44 ± 0.08	329.1	334.3	300
	R_C	337.1	20.39 ± 0.08	334.4	339.7	300
	R_C	379.6	20.85 ± 0.12	377.0	382.2	300
	R_C	384.9	20.69 ± 0.10	382.3	387.5	300
FTN	i'	7.41	16.05 ± 0.04	7.33	7.50	10
	i'	10.75	16.57 ± 0.04	10.50	11.00	30
	i'	15.93	17.06 ± 0.04	15.43	16.43	60
	i'	26.28	17.61 ± 0.04	25.28	27.28	120
	i'	41.88	18.10 ± 0.04	40.38	43.38	180
	i'	54.95	18.28 ± 0.05	53.95	55.95	120
	i'	105.2	18.82 ± 0.07	104.7	105.7	60
	i'	130.3	19.03 ± 0.06	129.3	131.3	120
	i'	200.7	19.39 ± 0.05	198.1	203.3	300
	i'	206.1	19.53 ± 0.06	203.5	208.7	300
	i'	224.6	19.55 ± 0.06	222.0	227.2	300
	i'	230.0	19.61 ± 0.06	227.3	232.6	300
	i'	248.5	19.73 ± 0.06	245.9	251.1	300
	i'	253.8	19.82 ± 0.07	251.2	256.4	300
	i'	292.3	20.06 ± 0.08	289.7	294.9	300
	i'	297.7	20.03 ± 0.08	295.1	300.3	300
	i'	319.8	20.11 ± 0.09	317.2	322.4	300
	i'	325.1	20.19 ± 0.09	322.5	327.7	300
	i'	343.7	20.20 ± 0.10	341.1	346.3	300
	i'	349.0	20.20 ± 0.10	346.4	351.6	300
i'	389.8	20.56 ± 0.25	389.0	390.6	100	
i'	395.1	20.10 ± 0.17	394.3	395.9	100	
FTN	B	5.98	16.87 ± 0.07	5.90	6.07	10
	B	8.52	17.50 ± 0.07	8.27	8.77	30
	B	12.25	17.95 ± 0.07	11.75	12.75	60
	B	18.22	18.34 ± 0.06	17.22	19.22	120
	B	30.35	18.85 ± 0.07	28.85	31.85	180
	B	46.42	19.32 ± 0.08	45.42	47.42	120
	B	59.55	19.56 ± 0.08	58.05	61.05	180
	B	139.8	20.27 ± 0.11	138.3	139.8	180
FTN	V	6.58	16.76 ± 0.06	6.50	6.67	10
TLS	R_C	599.4	20.87 ± 0.33	572.7	626.0	2400
	R_C	642.8	21.06 ± 0.18	626.8	658.7	1800
	R_C	675.4	21.11 ± 0.17	659.6	691.2	1800
	R_C	707.8	21.15 ± 0.15	692.0	723.7	1800
	R_C	740.3	21.32 ± 0.20	724.5	756.1	1800
	R_C	799.8	21.44 ± 0.29	778.6	821.0	2400
	R_C	1159	21.99 ± 0.29	1143	1175	1800
	R_C	1202	21.61 ± 0.30	1175	1229	3000
R_C	2806	22.51 ± 0.59	2776	2836	3600	
SARA	R_C	49.80	18.64 ± 0.06	47.30	52.30	300
	R_C	54.90	18.72 ± 0.08	52.40	57.40	300
	R_C	60.05	18.83 ± 0.07	57.55	62.55	300
	R_C	65.13	19.10 ± 0.13	62.63	67.63	300
	R_C	70.25	19.15 ± 0.11	67.75	72.75	300

Telescope	Filter	ΔT_{mean} (min)	Mag \pm Err	T_{start} (min)	T_{end} (min)	T_{exp} (s)
SARA	R_C	75.38	19.08 \pm 0.10	72.88	77.88	300
	R_C	80.51	19.28 \pm 0.17	78.01	83.01	300
	R_C	85.62	19.34 \pm 0.18	83.12	88.12	300
	R_C	90.77	19.30 \pm 0.20	88.27	93.27	300
	R_C	95.85	19.86 \pm 0.35	93.35	98.35	300
	R_C	101.2	19.53 \pm 0.31	98.65	103.7	300
	R_C	106.3	19.13 \pm 0.19	103.8	108.8	300
	R_C	111.4	20.31 \pm 0.40	108.9	113.9	300
	R_C	121.6	19.48 \pm 0.23	119.1	124.1	300
	R_C	126.8	19.39 \pm 0.21	124.3	129.3	300
	R_C	137.0	19.61 \pm 0.19	134.5	139.5	300
	R_C	142.1	19.90 \pm 0.19	139.6	144.6	300
	R_C	147.2	19.40 \pm 0.10	144.7	149.7	300
	R_C	152.5	19.53 \pm 0.17	150.0	155.0	300
	R_C	157.6	19.57 \pm 0.18	155.1	160.1	300
	R_C	162.8	19.65 \pm 0.20	160.3	165.3	300
	R_C	173.0	19.65 \pm 0.20	170.5	175.5	300
	R_C	178.1	19.96 \pm 0.29	175.6	180.6	300
	R_C	183.3	20.56 \pm 0.35	180.8	185.8	300
	R_C	193.5	19.76 \pm 0.17	191.0	196.0	300
	R_C	198.6	21.07 \pm 0.50	196.1	201.1	300
	R_C	203.9	20.11 \pm 0.21	201.4	206.4	300
	R_C	219.2	19.85 \pm 0.17	216.7	221.7	300
	R_C	224.4	19.85 \pm 0.16	221.9	226.9	300
	R_C	229.5	20.76 \pm 0.37	227.0	232.0	300
	R_C	234.6	20.41 \pm 0.25	232.1	237.1	300
R_C	239.7	20.17 \pm 0.22	237.2	242.2	300	
R_C	244.9	19.80 \pm 0.17	242.4	247.4	300	
R_C	250.0	19.92 \pm 0.24	247.5	252.5	300	
R_C	255.3	19.71 \pm 0.25	252.8	257.8	300	
R_C	260.4	19.76 \pm 0.42	257.9	262.9	300	
ST	R_C	934.4	21.21 \pm 0.07	919.0	946.1	1200
	R_C	1039	21.35 \pm 0.11	1024	1054	1800
	R_C	1136	21.61 \pm 0.13	1121	1151	1800
ST	I	958.5	21.02 \pm 0.21	948.5	968.5	1200
	I	1012	21.21 \pm 0.28	1002	1022	1200
	I	1103	21.28 \pm 0.22	1088	1118	1800
ST	V	985.2	21.53 \pm 0.13	970.2	1000	1800
	V	1071	21.63 \pm 0.12	1056	1086	1800
HCT	R_C	593.4	21.23 \pm 0.12	578.3	604.6	1080
	R_C	619.1	21.34 \pm 0.12	607.8	630.5	1200
HCT	B	658.3	21.74 \pm 0.08	633.5	682.9	2700
	B	728.3	22.09 \pm 0.10	685.9	770.8	4500
MAO	R_C	638.5	21.01 \pm 0.09	623.5	653.9	1200
	R_C	668.8	21.16 \pm 0.10	654.5	682.9	1500
	R_C	825.7	21.51 \pm 0.11	811.5	840.9	1500
	R_C	868.8	21.58 \pm 0.10	842.0	895.8	2700
OSN	I	757.7	20.68 \pm 0.08	730.0	783.3	2700
LT	r'	2233	21.69 \pm 0.15	2218	2247	1500
	r'	2289	22.17 \pm 0.12	2248	2329	4800
	r'	2669	22.34 \pm 0.08	2539	2763	10800
LT	i'	2343	21.76 \pm 0.17	2333	2354	1200
	i'	2490	21.95 \pm 0.20	2459	2520	3600
INT	r'	770.4	21.33 \pm 0.14	762.3	778.6	900
	r'	1171	21.60 \pm 0.05	1166	1176	900
	r'	2537	22.49 \pm 0.06	2525	2548	1200
	r'	5404	23.70 \pm 0.14	5390	5418	1200
INT	i'	753	21.07 \pm 0.22	744.6	760.9	900
	i'	1156	21.34 \pm 0.17	1148	1164	900
	i'	2565	22.21 \pm 0.06	2549	2580	1500
INT	i'	5431	23.08 \pm 0.11	5420	5443	1200
	g'	2593	22.96 \pm 0.06	2581	2604	1200
	g'	5457	23.91 \pm 0.11	5445	5468	1200
Gemini North	r'	5993	23.78 \pm 0.09	5990	5996	360
	r'	21606	24.61 \pm 0.14 ^a	21602	21609	360
Gemini North	i'	5985	23.46 \pm 0.14	5982	5989	360
Gemini North	g'	6002	24.14 \pm 0.09	5998	6007	480

^ahost galaxy dominated